Granular Matter (2022) 24:123
https://doi.org/10.1007/s10035-022-01283-x

ORIGINAL PAPER

Modelling the final discharge angle in flighted rotary drums

J. Seidenbecher[1] · F. Herz[1,2] · K. R. Sunkara[1] · J. Mellmann[3]

Received: 16 September 2021 / Accepted: 12 September 2022 / Published online: 14 October 2022

Abstract

Rotary drums equipped with longitudinal flights are mainly used to dry granular solids and handle high throughputs. The design of the flights is a crucial task because they decisively influence the distribution of the particles over the dryer cross section. In a previous work, the authors derived a mathematical model for the particle flow in rotary drums with rectangular flights. In this model, the final discharge angle was underpredicted resulting in errors when calculating the contact area of the particles in the air-borne phase. Therefore, a new model was developed in this study to predict the final discharge angle based on a forces balance approach on a single particle. This approach includes the Coriolis force acting on the last discharging particles sliding down the inclined flight sheet. The model was solved by using the vector analysis method. Experiments were performed at rotary drums with 0.5 m and 1.0 m in diameter, respectively, and 0.15/0.3 m in length using glass beads and quartz sand as bed materials. Each drum was equipped with 12 flights around the shell. The model validation was performed by varying the bed material, drum diameter, flight length ratio, and the rotating speed. The model predictions have shown that as the flight length ratio and the Froude number increased, the final discharge angle attained higher values. The model predictions agree well with the measurements.

Keywords Rotary drum · Flights · Transverse particle motion · Forces balance model · Vector analysis · Final discharge angle

List of symbols

d_P	Particle diameter (m)
D	Drum diameter (m)
f_D	Drum filling degree (–)
F_F	Frictional force (N)
F_G	Gravitational force (N)
F_N	Normal force (N)
F_x	Force in x direction (N)
F_y	Force in y direction (N)
Fr	Froude number (–)
Fr_C	Critical Froude number (–)
g	Acceleration due to gravity (m/s^2)
h_F	Height of fall (m)
$\vec{i}$	Unit vector along the rotating x axis (–)
$\vec{I}$	Unit vector along the x axis (–)
$\vec{j}$	Unit vector along the rotating y axis (–)
$\vec{J}$	Unit vector along the y axis (–)
l_1	Radial length of the flight (m)
l_2	Tangential length of the flight (m)
l_2/l_1	Flight length ratio (–)
L	Drum length (m)
m_P	Particle mass (kg)
n	Rotational speed (rpm)
n_F	Number of installed flights (–)
o	Intersection of the radial and tangential flight length (–)
oxy	Coordinates of a rotating frame (–)
O	Coordinate of the drum center (–)
OXY	Coordinates of a fixed frame (–)
$\vec{r}$	Position vector of the particle (–)
$\vec{r}_H$	Position vector of the origin (–)
r_H	Distance from the drum center to l_1 (m)
r_{HS}	Distance from the drum center to the tip of the flight (m)
r_P	Particle radius (m)
R	Drum radius (m)

✉ J. Seidenbecher
Jakob.Seidenbecher@Gmail.Com

F. Herz
fabian.herz@hs-anhalt.de

[1] Otto von Guericke University Magdeburg, Universitätsplatz 2, 39106 Magdeburg, Germany

[2] Anhalt University of Applied Sciences, 06366 Köthen, Germany

[3] Leibniz Institute for Agricultural Engineering and Bioeconomy (ATB), Max-Eyth-Allee 100, 14469 Potsdam, Germany

x_P^* Dimensionless x coordinate of the particle related to the drum radius (–)
y_P^* Dimensionless y coordinate of the particle related to the drum radius (–)

Greek letters

α Flight angle, (rad) see Fig. 4
α_{tan} Angle of the tangential flight length to the horizontal (rad)
β Flight angle, (rad) see Fig. 4
γ Kinetic angle of repose (rad)
γ_L Kinetic angle at the final discharge point (rad)
δ Discharge angle (circumferential position of the flight) (rad)
δ_L Final discharge angle (circumferential position of the flight at the final discharge) (rad)
$\delta_{L,exist}$: Final discharge angle according to an already existing model (rad)
θ Dynamic angle of repose (rad)
μ Coefficient of friction (–)
μ_W Particle–wall friction coefficient (–)
ρ_B Bulk density (kg/m^3)
φ_i Particle–particle (internal) friction angle (rad)
φ_W Particle–wall friction angle (rad)
χ Circumferential position of the radial flight length (rad)
χ_{init} Initial circumferential position of the radial flight length (rad)
ω Angular velocity (rad/s)

1 Introduction

Rotary drums installed with internal flights are most commonly used for drying or cooling of solids. The rotary drums are slightly inclined towards the horizontal and rotate around their own axis, while the wet feed is passed at the upstream end and the dried product is collected at the discharge end [1, 2]. These drums are fitted with a series of flights attached to the inner shell to distribute the solids across the free gas zone [3–6]. Three different phases of particle motion are identified in the drum cross section: flight borne solids, airborne solids, and dense phase of the bed at the bottom of the drum. The efficiency of the drum mainly depends on the extent of gas-solids contact in the airborne phase, which is mainly influenced by the flight design [7, 8]. The flight design determines the amount of material and its distribution in the airborne phase, which depends on the solids unloading rate of the flights and the final discharge angle (δ_L) [9–11]. Various studies were performed on the solids unloading rate thoroughly [12–21]. In previous studies, Sunkara et al. [9, 15] measured and modelled the flight filling degree and thus the flux of particles from a flight. So far, only a limited number of studies exist on the prediction of the final discharge angle, which is the angular position of the flight where the last particle leaves the flight sheet. However, the final discharge angle has significant importance for determining the quantity of particles in the airborne phase. As Sunkara [11] and Sunkara et al. [9, 15] have shown, the flight cascading rate and the height of fall of the particles are still at a high level in the final discharging range of the flights, depending on the flight length ratio l_2/l_1. Both parameters strongly affect the particle concentration in the curtains and, thereby, the heat and mass transfer in this part of the drum cross-section. The final discharge angle depends, among others, on the flight length ratio and the rotational speed, as can be seen in Fig. 1. The final discharge angle increases with both the flight length ratio and the rotational speed.

The surface of the packed bed in the flight is inclined to the horizontal by a certain angle. This angle depends on the circumferential position (δ) of the flight [10] and must therefore be distinguished from the dynamic angle of repose Θ of the bed at the bottom of the rotating drum, which is nearly constant in the rolling regime [22]. This angle of repose in the flights is referred to as the kinetic angle of repose (γ). Due to the continuous rotation of the drum, the orientation of the flight changes depending on its circumferential position. This is illustrated in Fig. 2. In the case of L-shaped flights, the tangential part of the flight is oriented vertically ($\alpha_{tan} = \pi/2$) after it has left the packed bed ($\delta = 0 + \alpha$). Here, α is the angle formed from the center of the rotary drum to the respective end points of the tangential flight sheet and thus depends on the flight length ratio. When the flight is at the top of the drum ($\delta = \pi/2 + \alpha$), the tangential portion of the flight is aligned horizontally ($\alpha_{tan} = 0$).

From this point, the angle of the tangential flight surface to the horizontal increases again. When the kinetic angle of repose of the particle bed in the flight is reached ($\alpha_{tan} = \gamma$), the final discharge takes place, which is illustrated in Fig. 3.

Based on the mathematical model from Schofield and Glikin [23] for calculating the kinetic angle of repose, Glikin [16] supposed that the flight empties when it is opposite to the bed at the bottom of the drum and the tangential flight sheet is in parallel to the surface of the bed. This approach was used by many authors [12, 24–26] to model the kinetic angle of repose. However, the final discharge angle also greatly depends on the rotational speed, and thus the Froude number, as well as on the flight length ratio/flight geometry [27], which has not been considered in the previous model of Schofield and Glikin.

The aim of the present work is to develop a mathematical model for predicting the final discharge angle of rectangular flights. For it, a balance of forces was derived on a single particle, which was solved using the vector analysis method. In this approach, the Coriolis force was included for the first

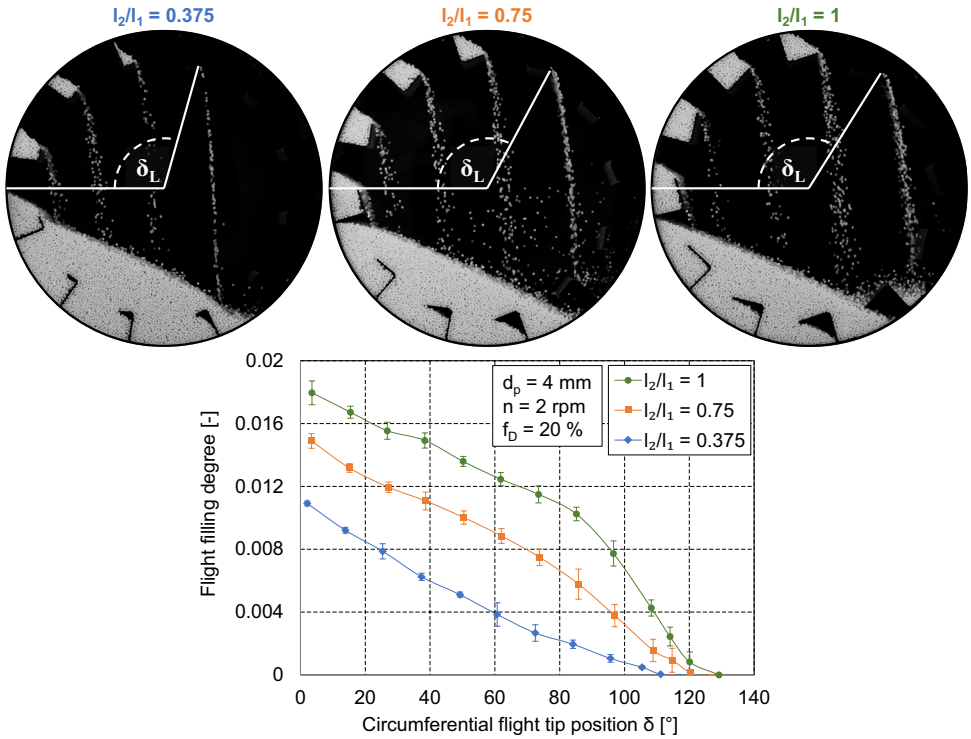

Fig. 1 Final discharge angles (δ_L) and measured flight filling degree versus circumferential flight tip position presented at different flight length ratios l_2/l_1 for drum diameter 0.5 m, 20 % filling degree, rotational speed 2 rpm, bed material 4 mm glass beads. The derivation of the flight filling degree provides the cascading rate of the flight. Both were modelled by Sunkara et al. [9, 15]

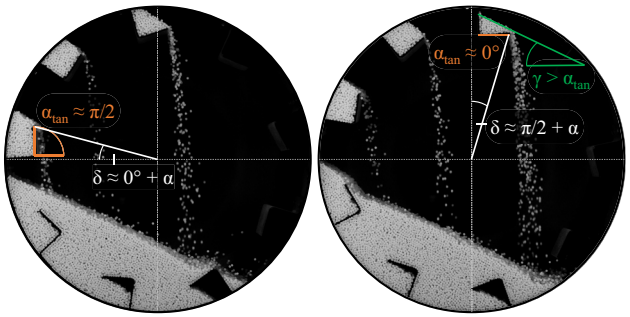

Fig. 2 Changing inclination (α_{tan}) of the tangential flight sheet in dependence on the circumferential position (δ)

time acting on the last discharging particles sliding down the inclined flight sheet. To validate the model, particle flow experiments were conducted at flighted laboratory drums using two different bed materials (glass beads and quartz sand). Besides the bed material, the influence of the geometrical parameters drum diameter and flight length ratio and the operational parameter rotational speed was investigated.

2 Modelling the final discharge angle

2.1 Particle discharge from the flight

The dimensionless parameters used in this study for the rotary drum with rectangular flights are described as follows. The flight's radial (l_1) and tangential length (l_2) are the typical flight dimensions as shown in Fig. 4.

The effective dimensionless radial distance (r_H) of the flight is given by

$$\frac{r_H}{R} = 1 - \frac{l_1}{R}, \tag{1}$$

where R is the radius of the drum. The characteristic angle made by the tangential flight length (l_2) to the effective radius of the flight (r_H) is

$$\tan \alpha = \frac{l_2}{r_H}. \tag{2}$$

The ratio between l_2 and l_1 is given as

$$\tan \beta = \frac{l_2}{l_1}. \tag{3}$$

The flight tip radius (r_{HS}) is defined by the following equation

$$r_{HS} = \frac{r_H}{\cos \alpha}. \tag{4}$$

The Froude number (Fr) relates the centrifugal force acting on the particles in the rotary drum to the gravitational force as

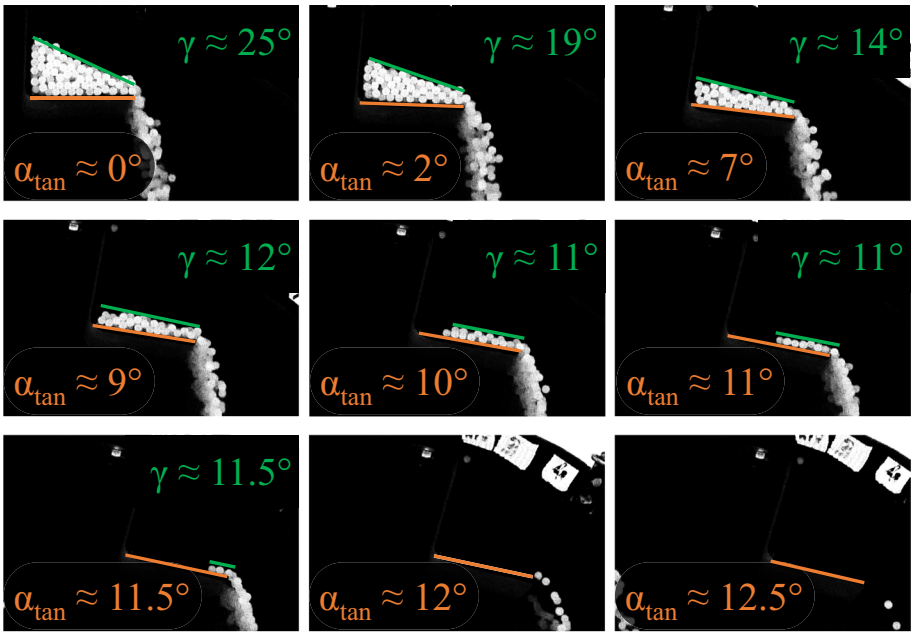

Fig. 3 Increasing angle of the tangential flight sheet to the horizontal α_{tan}; as the kinetic angle of repose is reached ($\alpha_{tan} = \gamma$), the final discharge takes place

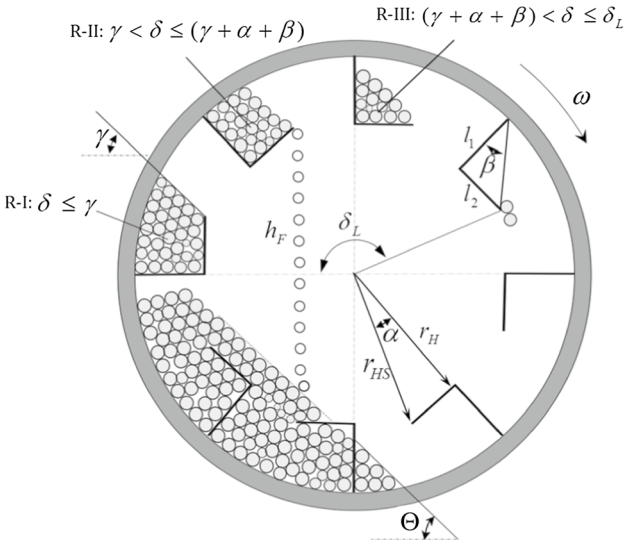

Fig. 4 Schematic diagram of a flighted rotary drum and the relevant geometric parameters; three circumferential regions (R-I/R-II/R-III) are distinguished with regard to the discharge behavior of the flights, figure taken from [9, 15]

$$Fr = \frac{\omega^2 R}{g}, \tag{5}$$

where ω is the angular velocity of the drum. In bulk mechanics, the angle of repose is known as the surface angle of a bed material, which is generated with the horizontal while forming a heap on a flat ground. While in a rotating drum, the surface angle formed by the bed material to the horizontal is termed as the dynamic angle of repose (Θ). In contrast to that, in flighted rotating drums the kinetic angle of repose (γ), which is formed by material in the flight with the horizontal, moreover depends on the flight's circumferential position (δ). According to Schofield and Glikin [23], the particles rolling down the surface of the particle bed in the flight are influenced by gravitational, centrifugal, and frictional forces. From this forces balance, the kinetic angle of repose is calculated as

$$\tan\gamma = \frac{\mu\cos\alpha + Fr\left(\frac{r_H}{R}\right)(\cos\delta - \mu\sin\delta)}{\cos\alpha - Fr\left(\frac{r_H}{R}\right)(\sin\delta - \mu\cos\delta)}, \tag{6}$$

where the coefficient of friction between the particles μ was assumed to be the tangent of the "angle of repose" [23]. The inertial forces acting on the moving particles based on Newton's second law and the Coriolis force were neglected. In Eq. (6), the kinetic angle γ approaches the (dynamic) angle of repose as the Froude number approaches to zero. The unloading of the flight occurs immediately after the flight is fully saturated by the bed material and it ends at a certain position—the final discharge angle ($\delta_L < \pi$).

2.2 Existing final discharge angle model

For a proper design of the drying or cooling process, the material-dependent discharging behavior of the flights must be known which includes a correct prediction of the final discharge angle. The target is that the particle curtains cover the entire cross section of the drum. As was shown by Sunkara [11] and Sunkara et al. [9, 15], the flight cascading rate and the height of fall of the particles are still at a high level in the final discharging range of the flights, depending on

the flight length ratio l_2/l_1. Both parameters strongly affect the particle concentration in the curtains and, thereby, the heat and mass transfer in this part of the drum cross-section. Hence, the prediction of the final discharge angle is of high relevance affecting the process and product quality after all. It depends on several parameters, such as the flight profile, rotational speed, and bed material properties. As described by Kelly [28], for a complex flight configuration like equal angular distribution (EAD), the kinetic angle of repose can be higher. The higher this angle, the higher is the number of particles contacting the hot gas.

Towards the point of final discharge, the amount of material in the flight is getting lower and lower, reaching a single layer in the final stage. This can be expected when the bed material has free-flowing behavior as is clearly visible in Fig. 3 for glass beads. In this stage, it is assumed that the particles are only subjected to frictional forces between the particles and between particles and the flight sheet as well as to collisional stresses between them. The particles roll/slide over the flight sheet surface under such conditions. Principally, the flight empties at a point given by the following equation [6, 16, 29, 30]

$$\delta_{L,exist} = \frac{\pi}{2} + \alpha + \gamma, \tag{7}$$

where the kinetic angle at the final discharge point was assumed to be $\gamma\left(\delta = \delta_{L,exist}\right) = \Theta$ by these authors.

Knowing that, besides the flight geometry and Froude number, the kinetic angle of repose γ varies in dependence on the angular position δ of the flight. Mellmann and Specht [31] concluded that, even at the final discharge point, the kinetic angle cannot be a constant as assumed in previous studies. They supposed that, at the final discharge point, the kinetic angle γ_L is a function of the flight geometry and the Froude number as well. For this reason, they extended Eq. (7) for the final discharge angle as

$$\delta_{L,exist} = \frac{\pi}{2} + \alpha + \gamma_{L.} \tag{8}$$

According to this approach, both angles—the kinetic angle γ_L and the angular position of the flight at the final discharge point $\delta_{L,exist}$—depend on each other. In order to calculate these values, two equations are required. By inserting Eq. (8) into Eq. (6) as

$$\tan\gamma_L = \frac{\mu\cos\alpha + Fr\left(\frac{r_H}{R}\right)\left[\cos\left(\pi/2+\alpha+\gamma_L\right) - \mu\sin\left(\pi/2+\alpha+\gamma_L\right)\right]}{\cos\alpha - Fr\left(\frac{r_H}{R}\right)\left[\sin\left(\pi/2+\alpha+\gamma_L\right) - \mu\cos\left(\pi/2+\alpha+\gamma_L\right)\right]} \tag{9}$$

Mellmann and Specht [31] obtained an equation for γ_L. Equation (9) can be solved only by iteration procedure. After calculation of γ_L, the final discharge angle $\delta_{L,exist}$ can be determined from Eq. (8).

2.3 Extended model for the final discharge angle

2.3.1 Assumptions

During the period of final discharge, the bed height in the flight decreases as the holdup of the flight tends to zero. As a result, the material in the static bed of the flight flowing into the active layer continuously decreases, which then leads to lower cascading rates. At a certain point, no active layer forms any more near the bed surface, and the material starts flowing down the inclined flight sheet as a whole in a diluted sliding or slipping layer. Finally, the thickness of this layer reduces to a one-particle layer (Fig. 3). A balance of forces was derived acting on the last discharging particle of this layer, which considers the Coriolis force. The following assumptions are made for the subsequent modeling:

- a simplified macroscopic model is developed,
- a single layer of particles flows down the inclined flight sheet,
- the particle–particle (internal) friction angle was assumed to be nearly equal to the dynamic angle of repose $\varphi_i \approx \Theta$, which is only valid for free-flowing non-cohesive bulk materials [32],
- for a rough estimation, the particle–wall friction angle φ_w was assumed to be equal to the particle–particle friction angle ($\varphi_w \approx \varphi_i$), which is valid for fine materials [32],
- no rolling friction between the particle and the flight sheet is considered, as for the used glass beads the coefficient of rolling friction on steel flights is negligibly small compared to the dynamic particle–wall friction coefficient [33] and
- the initial condition from the previous model is applied for this model.

For microscopic models using DEM, see Komossa et al. [33, 34] and Zhang et al. [35].

2.3.2 Rotating flight frame of reference

Consider a layer of particles on the flight surface that are ready to slide downwards to the flight tip as shown in Fig. 5.

Hence, the final discharge angle can be determined by predicting the position of the last particle (P) that leaves the flight surface. Consider oxy being a rotating frame of the flight which is moving around a fixed frame OXY. In Fig. 5, 'o' is the intersection of the radial (l_1) and tangential sheet (l_2) of the flight, and 'O' is fixed at the center of the drum. Let $\vec{I}$ and $\vec{J}$ be the unit vectors along the X and Y axes, and $\vec{i}$ and $\vec{j}$ are the unit vectors of the x and y axes. $\vec{r}$ is the position vector of the particle (P), and χ represents the circumferential position of the radial flight sheet. Based on the vector analysis, which is specified in the appendix, and

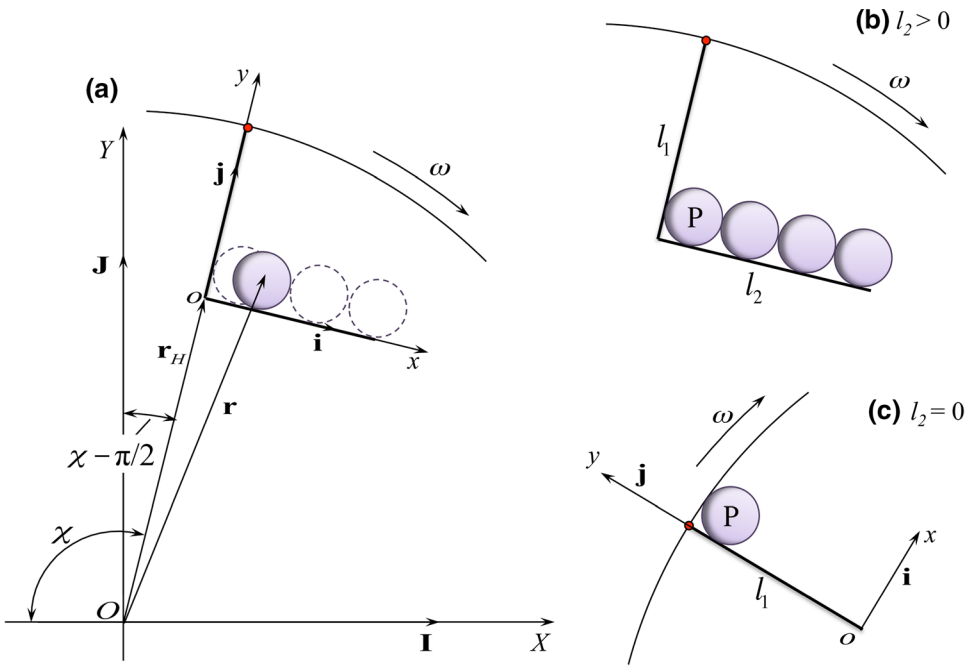

Fig. 5 Schematic of the rotating frame of a flight. **a** Geometric properties at the moment of the final discharge. **b** Final discharge and last particle (P) at the flight with a tangential component ($l_2 > 0$), **c** final discharge and last particle (P) in a flight assumed without a tangential component ($l_2 = 0$)

using Newton's second law of motion, the sum of the forces acting on a particle is expressed as

$$\sum \vec{F} = m_p\left[\frac{\Delta^2\vec{r}}{\Delta t^2} - \left(\boldsymbol{\omega}\times\frac{\Delta\vec{r}}{\Delta t}\right) - \left(\boldsymbol{\omega}\times\frac{\Delta\vec{r}}{\Delta t}\right) - \left(\frac{\Delta\boldsymbol{\omega}}{\Delta t}\times\vec{r}\right) + \left(\boldsymbol{\omega}\times(\boldsymbol{\omega}\times\vec{r})\right)\right], \tag{10}$$

expanding the fourth term in this equation as $\boldsymbol{\omega}\times\left(\boldsymbol{\omega}\times\vec{r}\right) = \left(\boldsymbol{\omega}\cdot\vec{r}\right)\boldsymbol{\omega} - (\omega\cdot\omega)\vec{r} = -\omega^2\vec{r}\ \left(\boldsymbol{\omega}\cdot\vec{r} = 0\right)$. By substituting the above equation and $\frac{\Delta\boldsymbol{\omega}}{\Delta t} = \dot{\boldsymbol{\omega}}$ in Eq. (10), the final form of the forces balance equation becomes

$$\sum \vec{F} = m_p\left[\frac{\Delta^2\vec{r}}{\Delta t^2} - 2\left(\boldsymbol{\omega}\times\frac{\Delta\vec{r}}{\Delta t}\right) - \left(\dot{\boldsymbol{\omega}}\times\vec{r}\right) - \boldsymbol{\omega}^2\vec{r}\right]. \tag{11}$$

The second and fourth terms in the right-hand side of Eq. (11) represent apparent forces, where $-2m_p\left(\boldsymbol{\omega}\times\frac{\Delta\vec{r}}{\Delta t}\right)$ is called Coriolis force and $-m_p\boldsymbol{\omega}^2\cdot\vec{r}$ represents the centrifugal force. To an observer at the moving frame, the Coriolis force acts perpendicularly to the direction of the moving object. Whereas the third term in the equation becomes ($\dot{\boldsymbol{\omega}} = 0$), since the rotating frame of the flight is moving at a constant angular velocity.

2.3.3 Describing the relative motion between particle and flight

Now, the equations are applied to the problem of particle sliding over the rotating flight. Let x_p and y_p represent the position of the particle relative to the moving frame of the flight. Assuming that the particle always contacts the flight sheet surface, $y_p = r_p$, where r_p is the radius of the particle, leeds to the following expression

$$\vec{r} = x_p\vec{i} + \left(y_p + r_H\right)\vec{j};\ \frac{\Delta\vec{r}}{\Delta t} = \dot{x}_p\vec{i} + \dot{y}_p\vec{j} = \dot{x}_p\vec{i};\ \frac{\Delta^2\vec{r}}{\Delta t^2} = \ddot{x}_p\vec{i}, \tag{12}$$

which results form of Eq. (27) (see Appendix). The sum of forces acting on the particle sliding over the flat surface inclined to the horizontal can be represented as

$$\sum \vec{F} = \sum F_x\vec{i} + \sum F_y\vec{j}. \tag{13}$$

Therefore, by resolving the forces components from Fig. 6 that act on the particle as it glides over the flight surface, we get

$$\begin{aligned}\sum F_x &= -\left(F_G\cos\chi - F_F\right)\\ \sum F_y &= -\left(F_N - F_G\sin\chi\right),\end{aligned} \tag{14}$$

where F_G is the gravitational force and F_F and F_N are the frictional and normal forces, respectively, acting on the particle. Simplifying Eqs. (11), (12) and (13) results in

$$\sum F_x\vec{i} + \sum F_y\vec{j} = m\left(\ddot{x}_p\vec{i} - 2\omega\dot{x}_p\vec{j} - \omega^2\left(x_p\vec{i} + \left(r_p + r_H\right)\vec{j}\right)\right). \tag{15}$$

The above equation is resolved into the respective components

$$\begin{aligned}\sum F_x &= m_p\left(\ddot{x}_p - \omega^2 x_p\right)\\ \sum F_y &= m_p\left(-2\omega\dot{x}_p - \omega^2\left(r_p + r_H\right)\right).\end{aligned} \tag{16}$$

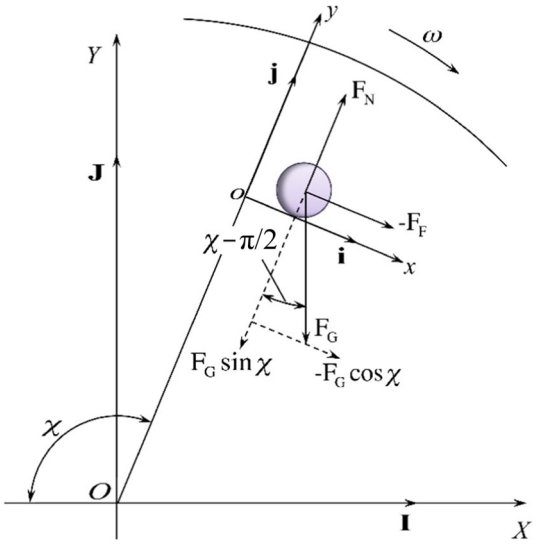

Fig. 6 Forces balance diagram of the particle sliding over the moving flight

Substituting Eq. (14) in Eq. (16) and rearranging the terms leads to

$$F_F = -m_p\ddot{x} \leq_p + m_p\omega^2 x_p - F_G\cos\chi$$
$$F_N = F_G\sin\chi - 2m_p\omega\dot{x}_p - m_p\omega^2\left(r_p + r_H\right). \tag{17}$$

Following Coulomb's law for the relation between the friction and normal forces and Eq. (17) as well as $\ddot{x}_p = \frac{\Delta^2 x_p}{\Delta t^2}$; $\dot{x}_p = \frac{\Delta x_p}{\Delta t}$; μ_w as the particle–wall friction coefficient ($\mu_w = \tan\varphi_w$) and $\Delta t = \frac{\Delta\chi}{\omega}$ results in

$$\omega^2\frac{\Delta^2 x_p}{\Delta\chi^2} - 2\mu_w\omega^2\frac{\Delta x_p}{\Delta\chi} - \omega^2 x_p = \mu_w\omega^2\left(r_p + r_H\right) - \mu_w g\sin\chi - g\cos\chi. \tag{18}$$

Divide the above equation with (ω^2R) to convert it into a dimensionless form to finally get

$$\frac{\Delta^2 x_p^*}{\Delta\chi^2} - 2\mu_w\frac{\Delta x_p^*}{\Delta\chi} - x_p^* = \mu_w\left(\frac{r_p + r_H}{R}\right) - \frac{1}{Fr}\left(\mu_w\sin\chi + \cos\chi\right), \quad \text{for} l_2 > 0, \tag{19}$$

where $x_p^* = \frac{x_p}{R}$. Equation (19) is valid when the length of the tangential sheet of the flight is $l_2 > 0$ (see Fig. 5b). However, a similar equation can be developed for the case of a drum with radial flights with $l_2 = 0$ (see Fig. 5c), where x_p is constant but y_p varies with time. Following the same procedure as above, the final equation for the particle position in radial flights can be written as follows

$$\frac{\Delta^2 y_p^*}{\Delta\chi^2} - 2\mu_w\frac{\Delta y_p^*}{\Delta\chi} - y_p^* = \left(\frac{r_p + r_H}{R}\right) - \frac{1}{Fr}\left(\mu_w\sin\chi + \cos\chi\right), \quad \text{for } l_2 = 0, \tag{20}$$

where $y_p^* = \frac{y_p}{R}$.

2.3.4 Solution of the final model equation

In order to solve Eq. (19), it has been transformed into two simultaneous differential equations by considering $x_p^* = x_1$, $\frac{\Delta x_p^*}{\Delta\chi} = x_2$ and $\frac{\Delta^2 x_p^*}{\Delta\chi^2} = \frac{\Delta x_2}{\Delta\chi}$. Substituting these terms in Eq. (19) to get the following equations

$$\frac{\Delta x_1}{\Delta\chi} = x_2$$
$$\frac{\Delta x_2}{\Delta\chi} = \left(2\mu_w x_2 + x_1\right) + \mu_w\left(\frac{r_p + r_H}{R}\right) - \frac{1}{Fr}\left(\mu_w\sin\chi + \cos\chi\right). \tag{21}$$

The initial conditions to solve the above equations are

$$\chi_{init} = \delta_L - \alpha = \frac{\pi}{2} + \gamma_L$$
$$x_1\big|_{\chi_{init}} = r_p/R \tag{22}$$
$$x_2\big|_{\chi_{init}} = 0$$

where δ_L is the final discharge angle considered from the previous model according to Eq. (8), and γ_L can be calculated from Eq. (9). For an observer in the rotating frame, $x_2\big|_{\chi_{init}} = 0$ since the velocity of the particle is zero before sliding occurs. These equations were solved in MATLAB using Runge–Kutta (ODE 45) method. After solution of the equation system (20) with (21), the final angular position of the radial flight sheet χ_L is calculated. From this value, the final discharge angle δ_L is obtained as

$$\delta_L = \chi_L + \alpha \tag{23}$$

3 Experimental investigations

The experimental setup used in the present study is shown in Fig. 7. The experiments were performed in two different drums with diameters of D = 500/1000 mm and lengths of L = 150/300 mm. Each drum is arranged in horizontal position in order to maintain uniform axial profiles. The front end of the drum is covered with glass, and a steel plate covers the back wall. The provision of the glass ensures that the videos of the experiments can be recoded in high quality.

A high definition camera was used to record the videos of the experiments and was placed perpendicular to the drum. The drum was initially furnished with $n_F = 12$ flights of

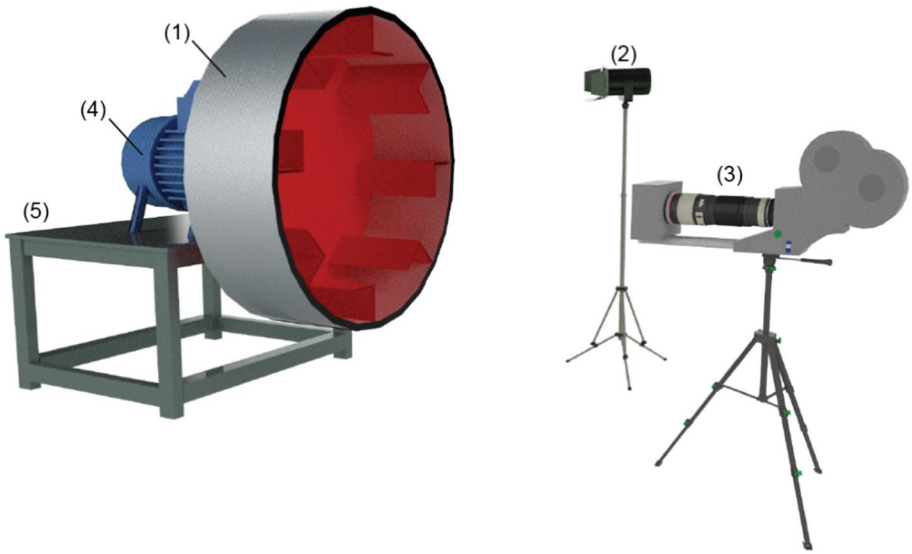

Fig. 7 Experimental setup: (1) experimental drum (D = 500 mm, L = 150 mm) (2) light (3) camera (4) electric motor (5) frame, figure taken from [9, 10, 15]

Table 1 Drum parameters and experimental settings

Parameter	Value
Drum diameter (D)	0.5 m; 1.0 m
Ratio (l_1/R)	0.2
Flight length ratio (l_2/l_1)	1.0; 0.75; 0.375; 0
Number of flights (n_F)	12
Rotation speed (n)	0.5–10 rpm
Drum filling degree ($f_{D)}$	0.2

Table 2 Properties of the bed materials used

Bed material	d_P (mm)	ρ_B (kg/m^3)	Θ (°)
Quartz sand	0.2	1570	32.4
Glass beads	0.7	1560	28.0

rectangular L-shape. The details of the experimental conditions employed in the current study are provided in Table 1. The experiments were performed with four different profiles of the rectangular flight by varying the flight length ratio (l_2/l_1) at 1.0, 0.75, 0.375, and 0. To adjust this ratio, the tangential length (l_2) of the flight was stepwise reduced, whereas the ratio of l_1/R was set constant at 0.2 for all experiments. The model has been validated for two different bed materials: namely quartz sand of $d_P = 0.2$ mm and glass beads of $d_P = 0.7$ mm particle diameter. The properties of the bed materials are listed in Table 2. The dynamic angle of repose of the bed materials was measured in a drum without flights operated at $f_D = 10$ % and Fr = 0.0007. In the particle flow experiments, the drum was operated at different rotational speeds (n = 0.5–10 rpm) and a drum filling degree of 20 %, so that it could be operated under over-loaded conditions. Each experimental setting was performed with all profiles of the flight. The experiments were recorded using a high definition camera. Single frames were collected from the videos and were evaluated in order to measure the kinetic angle of repose at the bed material surface of the flight.

4 Results and discussion

The new model for the final discharge angle according to Sect. 0 has been validated based on particle flow experiments, which were conducted in the flighted rotating drum (Fig. 7) using glass beads and quartz sand as bed materials, see Table 2. The drum was filled by 20 %. The experimental data were obtained by evaluating the images of several discharging flights and measuring the individual final discharge angles. After that, mean values were calculated of the final discharge angle for each experimental setting.

The results are shown in Figs. 8, 9 and 10, where the final discharge angle is depicted versus the Froude number for different flight length ratios of $l_2/l_1 = 0$, 0.375, and 1.0, respectively. In all cases, the particle-to-wall friction coefficient was calculated based on the assumption that $\varphi_W = \theta$. For comparison, also the calculations from the old model according to Eqs. (8) and (9) are illustrated. As can be seen from these graphs, the measurements indicate that the final discharge angle increases as the Froude number increases for all flight length ratios. Against it, the predictions of the old model show an inverse trend meaning that the flight is discharging at significantly lower angles. The new model well predicts the measured trend of increasing final discharge angles as the Froude number increases. Figures 9 and 10 show a good agreement between experimental and simulated

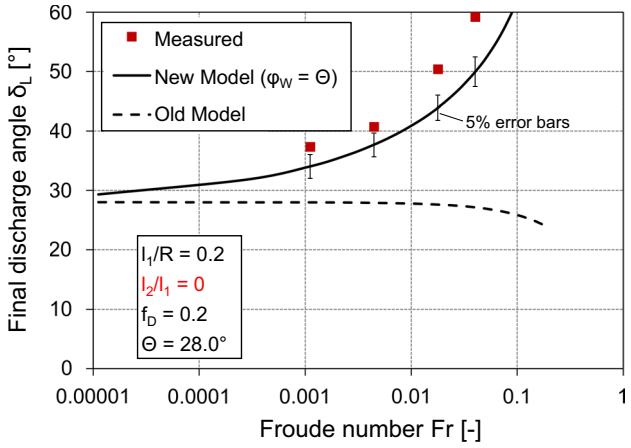

Fig. 8 Model validation: comparison between measured and predicted final discharge angles as a function the Froude numbers for glass beads (D = 500 mm, $l_2/l_1 = 0$)

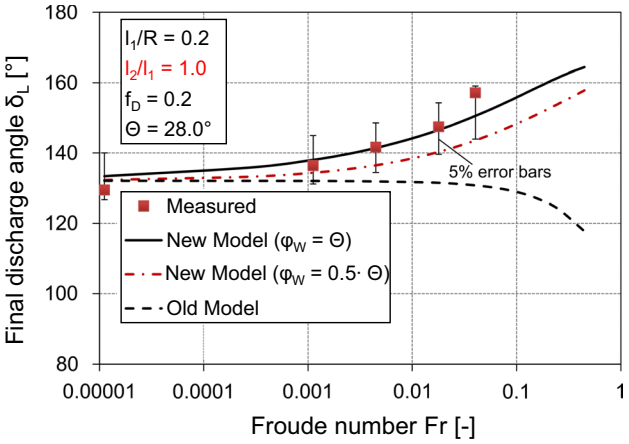

Fig. 10 Model validation: comparison between measured and predicted final discharge angles as a function the Froude numbers for glass beads (D = 500 mm, $l_2/l_1 = 1.0$)

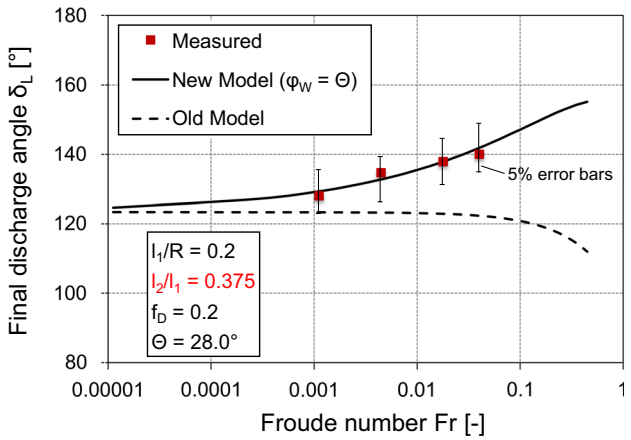

Fig. 9 Model validation: comparison between measured and predicted final discharge angles as a function the Froude numbers for glass beads (D = 500 mm, $l_2/l_1 = 0.375$)

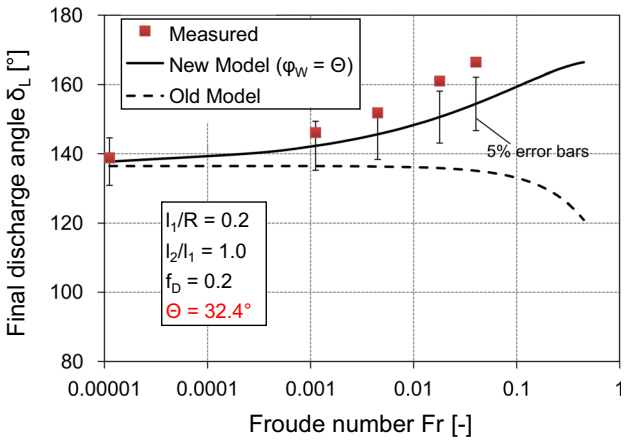

Fig. 11 Model validation: measured final discharge angles as compared to predicted values versus Froude number for quartz sand (D = 500 mm, $l_2/l_1 = 1.0$)

results of the new model for flight length ratios of 0.375 and 1.0, respectively. Except for the radial flight ($l_2/l_1 = 0$, see Fig. 8), the new model under-predicts the final discharge angle. In Fig. 10, the effect of a lower particle–wall friction coefficient was tested in the new model assuming that the wall friction angle is half of the dynamic angle of repose as $\varphi_W = 0.5 \cdot \Theta$. With it, the same tendency was predicted by the new model indicating that the discharge angle increases as the Froude number increases. However, the deviations from the measurements increased because this wall friction angle $\varphi_W = 0.5 \cdot \Theta$ is not realistic for the bed material used (glass beads).

In the next step, the new model was tested with another bed material, namely quartz sand. For quartz sand, higher final discharge angles were measured than for glass beads, as shown in Fig. 11. As the results show, the new model is able to predict the measured trend of the final discharge angle also for this bed material. At Froude numbers lower than about 0.005, the model well predicted the measured values and the simulated values fell into the 5 % error range. However, it increasingly deviated at higher Froude numbers.

Since the final discharge angle depends on the Froude number, it is a function of the drum dimensions as well. Therefore, the new model was then validated with respect to the drum diameter. For it, the bigger drum of 1000 mm in diameter (Table 1) was used with a flight length ratio of $l_2/l_1 = 0.75$, and the measurements were performed with glass beads. The results are shown in Fig. 12, where measured and predicted final discharge angles are depicted over the Froude number. It can be seen that the new model provides

a good prediction of the final discharge angle also at higher drum dimensions.

To verify the progress of the new model, the results from all experiments conducted in this study were considered and compared with the predictions from both models. In order to evaluate the degree of agreement, a linear regression was performed between measured and predicted results in each case. These comparisons are shown in Figs. 13 and 14 over the whole range of discharge angles between 0 and π.

As can be seen from the graphs, the new model can well predict the final discharge angle of rectangular flights with a coefficient of determination of $R^2 = 0.987$. This is a good result considering the wide range of experimental settings and the two different bed materials investigated. Almost all values fall into the 10 % error range, whereas for the old model the degree of agreement is considerably lower. Especially in the lower region of discharge angles (radial flights, $l_2/l_1 = 0$), the old model cannot predict reliable values of the final discharge angle.

As demonstrated, the new model for calculating the final discharge angle is able to predict the particle flow pattern of a discharging rectangular flight, which has already been observed by Sunkara et al. [9]. In this study, the simplified assumption was used that the particle-to-wall friction angle is equal to the dynamic angle of repose of the respective bed material ($\varphi_W = \Theta$). In further studies, it is intended using measured values of the particle–particle and particle–wall friction angles to reduce the number of model assumptions and to improve the new model. The results indicate that, from a certain point of discharge, the bulk material in the flight should be considered as diluted where the bed height has already dropped down to a low value. Hence, it is necessary to consider the transition from the dense phase to the dilute phase in the geometrical model.

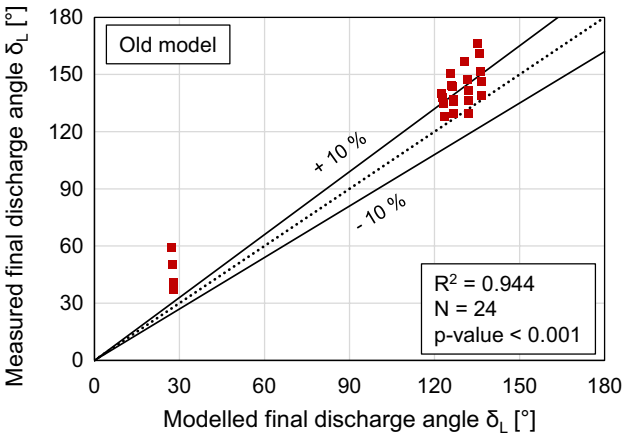

Fig. 13 Measured versus predicted final discharge angles calculated by the old model, see Eq. (9), linear regression over the whole range of measurements conducted in this study

However, this transition point is still unknown and needs further investigation.

5 Conclusion

A new geometric model has been developed to predict the final discharge angle of rectangular flights without adopting geometrical simplifications. In this model, besides Newton's second law of motion the Coriolis force was considered for the first time. In particular, the influence of the drum diameter, flight length ratio, rotational speed (Froude number), and the bed material on the final discharge angle was investigated. The measurements revealed that, as the flight length ratio and the rotational speed/Froude number

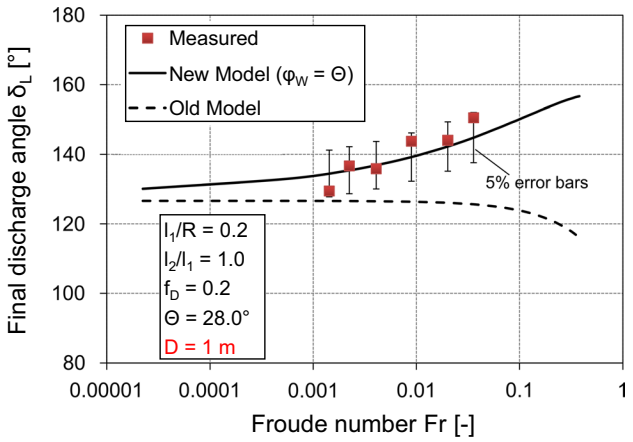

Fig. 12 Measured and predicted final discharge angles versus Froude number for glass beads and an increased drum diameter ($D = 1000$ mm; $l_2/l_1 = 0.75$)

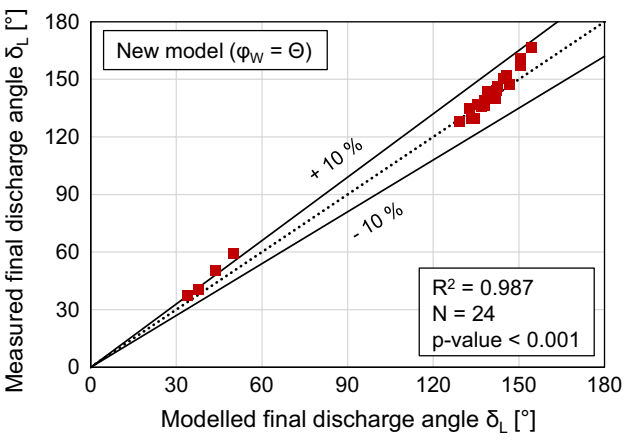

Fig. 14 Measured versus predicted final discharge angles calculated by the new model with $\varphi_W = \Theta$, linear regression over the whole range of measurements conducted

increased, the final discharge angle increased as well. The experiments were conducted in rotary drums with diameters of 500 mm and 1000 mm, respectively, using glass beads and quartz sand as bed materials. The larger the drum diameter, the larger the final discharge angle. The same trend was observed with respect to the dynamic angle of repose as a bed material property. A very good agreement was obtained between the measurements and the predictions with the new model. As compared to existing models that under-predict the range of flight discharge in the drum cross-section, the new model is able to calculate reliable values of the final discharge point. Integrating this new approach into a particle flow model of flighted rotary drums will, therefore, considerably improve the prediction of the surface area of the particles in the falling curtains responsible for heat and mass transfer. This model can also be used to scale the flight design from laboratory scale to production scale. And it can be easily extended to study the behavior of other types of flights.

Appendix

The unit vectors of the rotating frame $(\vec{i};\ \vec{j})$ can be expressed in terms of the fixed frame of reference $(\vec{I};\ \vec{J})$ from the triangular law of addition of vectors (see Fig. 5) as

$$\vec{i} = \sin\chi \cdot \vec{I} + \cos\chi \cdot \vec{J}; \vec{j} = -\cos\chi \cdot \vec{I} + \sin\chi \cdot \vec{J}. \tag{24}$$

The position vector of the particle can be expressed as

$$\vec{r} = X\vec{I} + Y\vec{J}, \tag{25}$$

where X and Y are the coordinates of the particle with respect to the fixed frame. Similarly, the position vector can also be expressed as a function of the rotating frame

$$\vec{r} = \vec{r}_H + \left(x\vec{i} + y\vec{j}\right), \tag{26}$$

with $\vec{r}_H$ as the position vector of the origin (o) follows

$$\vec{r} = x\vec{i} + \left(y + r_H\right)\vec{j}. \tag{27}$$

Hence, from this relation the velocity of the particle to an observer in the fixed frame of reference can be obtained by differentiating Eq. (25) with time

$$\frac{d\vec{r}}{dt} = \dot{X}\vec{I} + \dot{Y}\vec{J}. \tag{28}$$

However, to an observer in the rotating frame, the velocity of the particle can be written as

$$\frac{\Delta\vec{r}}{\Delta t} = \dot{x}\vec{i} + \dot{y}\vec{j}. \tag{29}$$

By differentiating Eq. (27), a relation for both frames can be developed using $\dot{\chi} = \omega$

$$\frac{d\vec{r}}{dt} = \frac{\Delta\vec{r}}{\Delta t} + \left[\left(y + r_H\right)\omega\vec{i} - x\omega\vec{j}\right] = \left(\frac{\Delta\vec{r}}{\Delta t} + \omega \times \vec{r}\right), \tag{30}$$

where $\boldsymbol{\omega} = \omega\vec{k}$ and with $\vec{k}$ as the unit vector orthogonal to $\vec{i}, \vec{j}$. Thus, the relation between the fixed frame of reference and the rotating frame can be written as

$$\frac{d}{dt} = \left(\frac{\Delta}{\Delta t} + \omega\times\right). \tag{31}$$

Funding Open Access funding enabled and organized by Projekt DEAL.

Declarations

Conflict of interest The authors declare the following financial interests/personal relationships which may be considered as potential competing interests.

References

1. Matchett, A.J., Baker, C.G.J.: Particle residence times in cascading rotary dryers. Part 1—derivation of the two-stream model. J. Sep. Process Technol. **8**, 11–17 (1987)
2. Friedman, S.J., Marshall, W.R.: Studies in rotary drying. 1. Holdup and dusting. Chem. Eng. Prog. **45**, 482–493 (1949)
3. Sherritt, R.G., Caple, R., Behie, L.A., Mehrotra, A.K.: The movement of solids through flighted rotating drums. Part I: Model formulation. Can. J. Chem. Eng. **71**, 337–346 (1993)
4. Britton, P.F., Sheehan, M.E., Schneider, P.A.: A physical description of solids transport in flighted rotary dryers. Powder Technol. **165**, 153–160 (2006)
5. Shahhosseini, S., Cameron, I.T., Wang, F.Y.: A simple dynamic model for solid transport in rotary dryers. Drying Technol. **18**, 867–886 (2000)
6. Baker, C.: The design of flights in cascading rotary dryers. Dry. Technol. **6**, 631–653 (1988)
7. Le Guen, L., Piton, M., Hénaut, Q., Huchet, F., Richard, P.: Heat convection and radiation in flighted rotary kilns: a minimal model. Can. J. Chem. Eng. **95**, 100–110 (2017)

8. Ajayi, O.O., Sheehan, M.E.: Design loading of free flowing and cohesive solids in flighted rotary dryers. Chem. Eng. Sci. **73**, 400–411 (2012)
9. Sunkara, K.R., Herz, F., Specht, E., Mellmann, J.: Influence of flight design on the particle distribution of a flighted rotating drum. Chem. Eng. Sci. **90**, 101–109 (2013)
10. Sunkara, K.R., Herz, F., Specht, E., Mellmann, J.: Transverse flow at the flight surface in flighted rotary drum. Powder Technol. **275**, 161–171 (2015)
11. Sunkara, K.R.: Granular Granular flow and design studies in flighted rotating drums. Dissertation, Magdeburg, (2013)
12. Lee, A., Sheehan, M.E.: Development of a geometric flight unloading model for flighted rotary dryers. Powder Technol. **198**, 395–403 (2010)
13. Karali, M.A., Sunkara, K.R., Herz, F., Specht, E.: Experimental analysis of a flighted rotary drum to assess the optimum loading. Chem. Eng. Sci. **138**, 772–779 (2015)
14. Karali, M.A., Specht, E., Herz, F., Mellmann, J., Refaey, H.A.: Unloading characteristics of flights in a flighted rotary drum operated at optimum loading. Powder Technol. **333**, 347–352 (2018)
15. Sunkara, K.R., Herz, F., Specht, E., Mellmann, J., Erpelding, R.: Modeling the discharge characteristics of rectangular flights in a flighted rotary drum. Powder Technol. **234**, 107–116 (2013)
16. Glikin, P.G.: Transport of solids through flighted rotating drums. Trans. Inst. Chem. Eng. **56**, 120–126 (1978)
17. Porter, S.J.: The design of rotary dryers and coolers. Transp. Inst. Chem. Eng. **41**, 272–287 (1963)
18. Kelly, J.J., O'Donnell, J.P.: Dynamics of granular material in rotary driers and coolers. Inst. Chem. Eng. Sym. Ser **29**, 34–44 (1968)
19. Karali, M.A., Specht, E., Mellmann, J., Refaey, H.A., Salem, M.R., Elbanhawy, A.Y.: Granular transport through flighted rotary drums operated at optimum-loading: mathematical model. Dry. Technol. **38**, 495–505 (2020)
20. Benhsine, I., Hellou, M., Lominé, F., Roques, Y.: Influence of flight shape on discharging profiles of granular material in rotary dryer. In: EPJ Web of Conferences (Vol. 140, p. 3023 (2017)
21. Debacq, M., Vitu, S., Ablitzer, D., Houzelot, J.-L., Patisson, F.: Transverse motion of cohesive powders in flighted rotary kilns: experimental study of unloading at ambient and high temperatures. Powder Technol. **245**, 56–63 (2013)
22. Mellmann, J.: The transverse motion of solids in rotating cylinders—forms of motion and transition behavior. Powder Technol. **118**, 251–270 (2001)
23. Schofield, F.R., Glikin, P.G.: Rotary dryers and coolers for granular fertilizers. Chem. Eng. Res. Des. **40**, 183–190 (1962)
24. Lisboa, M.H., Vitorino, D.S., Delaiba, W.B., Finzer, J.R.D., Barrozo, M.A.S.: A study of particle motion in rotary dryer. Braz. J. Chem. Eng. **24**, 365–374 (2007)
25. Hellou, M., Lominé, F., Benhsine, I., Roques, Y.: Theoretical description of the motion of a particle in rotary dryer. Can. J. Chem. Eng. **97**, 103–114 (2019)
26. Nascimento, S.M., Duarte, C.R., Barrozo, M.A.S.: Analysis of the design loading in a flighted rotating drum using high rotational speeds. Dry. Technol. **36**, 1200–1208 (2018)
27. Revol, D., Briens, C., Chabagno, J.: The design of flights in rotary dryers. Powder Technol. **121**, 230–238 (2001)
28. Kelly, J.: Flight design in rotary dryers. Dry. Technol. **10**, 979–993 (1992)
29. Blumberg, W., Schlünder, E.-U.: Transversale schüttgutbewegung und konvektiver stoffübergang in Drehrohren. Teil 2: Mit Hubschaufeln. Chem. Eng. Process. Process Intensif. **35**, 405–411 (1996)
30. van Puyvelde, D.R.: Modelling the hold up of lifters in rotary dryers. Chem. Eng. Res. Des. **87**, 226–232 (2009)
31. Mellmann, J., Specht, E.: Particle motion, filling degree and surface area of the flying curtain in cascading rotary dryers. In: EFCE Working Party on Drying, Magdeburg, Germany (2002)
32. Schubert, H.: Aufbereitung fester mineralischer Rohstoffe: Bd. III, VEB Deutscher Verlag für Grundstoffindustrie, Leipzig, (1984)
33. Komossa, H., Wirtz, S., Scherer, V., Herz, F., Specht, E.: Heat transfer in indirect heated rotary drums filled with monodisperse spheres: comparison of experiments with DEM simulations. Powder Technol. **286**, 722–731 (2015)
34. Komossa, H., Wirtz, S., Scherer, V., Herz, F., Specht, E.: Transversal bed motion in rotating drums using spherical particles: comparison of experiments with DEM simulations. Powder Technol. **264**, 96–104 (2014)
35. Zhang, L., Jiang, Z., Weigler, F., Herz, F., Mellmann, J., Tsotsas, E.: PTV measurement and DEM simulation of the particle motion in a flighted rotating drum. Powder Technol. **363**, 23–37 (2020)